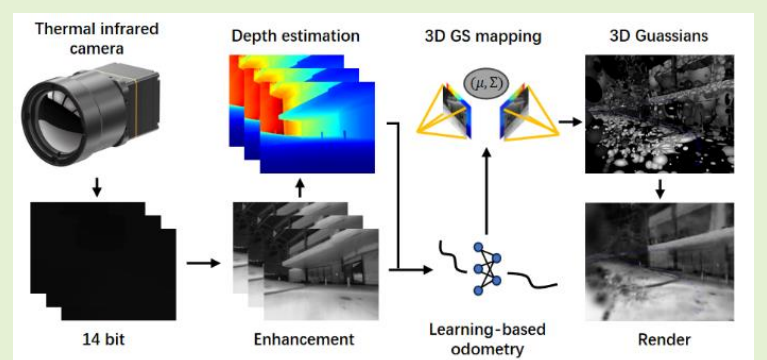


Thermal Odometry and Dense Mapping using Learned Odometry and Gaussian Splatting

Tianhao Zhou, Yujia Chen, Zhihao Zhan, Yuhang Ming, *Member, IEEE*, and Jianzhu Huai*, *Member, IEEE*

Abstract—Thermal infrared sensors, with wavelengths longer than smoke particles, can capture imagery independent of darkness, dust, and smoke. This robustness has made them increasingly valuable for motion estimation and environmental perception in robotics, particularly in adverse conditions. Existing thermal odometry and mapping approaches, however, are predominantly geometric and often fail across diverse datasets while lacking the ability to produce dense maps. Motivated by the efficiency and high-quality reconstruction ability of recent Gaussian Splatting (GS) techniques, we propose TOM-GS, a thermal odometry and mapping method that integrates learning-based odometry with GS-based dense mapping. TOM-GS is among the first GS-based SLAM systems tailored for thermal cameras, featuring dedicated thermal image enhancement and monocular depth integration. Extensive experiments on motion estimation and novel-view rendering demonstrate that TOM-GS outperforms existing learning-based methods, confirming the benefits of learning-based pipelines for robust thermal odometry and dense reconstruction.



Index Terms—Learning-based motion estimation, dense thermal mapping, Gaussian splatting, thermal infrared odometry, thermal SLAM

I. INTRODUCTION

Commercial thermal infrared sensors operate primarily in the long-wave infrared band (8–14 μm), making them inherently robust to low-light conditions[1], airborne dust[2], and smoke[3]. This resilience has led to widespread use in facility inspections and nighttime surveillance, and more recently, robotics. As robotic applications expand into visually degraded environments, thermal cameras have become attractive alternatives for simultaneous localization and mapping (SLAM)[4], offering strong potential for search and rescue, subterranean exploration, and firefighting.

A large body of work has explored thermal imagery for motion estimation by extending techniques originally designed for RGB cameras. For example, FirebotSLAM[3] adapts ORB-SLAM3[5] to stereo thermal cameras for motion estimation using SURF features[6]. In UAV odometry, a stereo thermal method[7] highlights the benefits of contrast en-

hancement and a double dogleg-based optimization strategy. Another study[8] based on libviso2[9] to tailor classical visual odometry to thermal inputs. MonoThermal-SLAM[10] extends ORB-SLAM2[11] by integrating line features and semantic segmentation to handle dynamic objects, resulting in a sparse landmark map. Building on this line of work, the authors later introduced an odometry method[12] that adapts SVO[13] for a custom catadioptric omnidirectional thermal camera. Additional efforts focus on addressing the inherent low texture and limited contrast of thermal images through edge-based feature extraction[14], [15] and non-uniformity correction (NUC)[8], [16]. While geometric SLAM systems such as ORB-SLAM3[3], VINS-Mono[1], and OKVIS[2] have achieved promising motion estimation using these enhanced images, conventional geometric pipelines remain fragile when applied to diverse and challenging datasets[17], [18].

Recent research has shifted toward learning-based thermal odometry and depth prediction[19], [20]. These approaches improve motion estimation but typically focus only on odometry, without producing dense maps that are essential for downstream tasks such as motion planning and reconstruction. While some methods incorporate additional sensors (e.g., RGB or LiDAR) to achieve dense mapping[21], [22], [23], these modalities often fail in adverse environments where thermal sensing excels. A thermal–radar fusion method[24] enables dense depth estimation, and a self-supervised thermal odometry framework[19] predicts monocular depth and pose,

Tianhao Zhou, Yujia Chen and Jianzhu Huai are with State Key Lab of Information Engineering in Surveying, Mapping, and Remote Sensing, Wuhan University, 129 Luoyu Road, Wuhan, Hubei 430079, China (email: zhoutianhao314@whu.edu.cn; 2023302081080@whu.edu.cn; jianzhu.huai@whu.edu.cn)

Zhihao Zhan is with TopXGun Robotics, Nanjing, Jiangsu 211100, China (email: zhihazhan2-c@my.cityu.edu.hk)

Yuhang Ming is with School of Computer Science, Hangzhou Dianzi University, Hangzhou, Zhejiang 310018, China (email: yuhang.ming@hdu.edu.cn)

*Corresponding author: Jianzhu Huai

but these pipelines still produce sparse maps or rely heavily on auxiliary sensors.

In parallel, learning-based visual odometry (VO) has advanced rapidly. For example, DROID-SLAM[18] supports monocular, stereo, and RGB-D inputs, achieving state-of-the-art dense tracking. Follow-up works have further enhanced semantic understanding[25], dynamic object handling, and memory efficiency[26].

For dense mapping, neural rendering has emerged as a compelling alternative to geometric methods by learning continuous scene representations. NeRF[27], in particular, has accelerated research in dense mapping and pose refinement. Systems such as VoxFusion[28] demonstrate joint pose-map optimization, while other pipelines use NeRF exclusively for mapping with separate tracking modules, as seen in NeRF-SLAM[29], GLORIE-SLAM[30], and NeRF-VO[31] built on learned odometry methods like DROID-SLAM[18] and DPVO[26].

To enhance rendering and training efficiency, 3D Gaussian Splatting (GS)[32] has recently become a strong competitor to NeRF[27]. GS-based representations have been applied to dense mapping in methods such as 2DGGS[33] and AbsGS[34], and to integrated odometry–mapping systems such as MonoGS[35] and SplatTAM[36]. Several recent 3DGGS-based SLAM frameworks adopt a decoupled architecture, separating tracking and mapping while using 3D Gaussians for dense representation. Representative systems include PhotoSLAM[37], TAMBRIDGE[38], and Splat-SLAM[39]. While GS-based mapping has shown substantial progress in RGB-based SLAM, its use with coarse, low-texture thermal imagery remains largely unexplored.

Motivated by the limitations of existing thermal SLAM approaches and the rapid progress in GS-based methods, this paper presents a learning-based thermal odometry and mapping system for monocular thermal sequences. The proposed thermal SLAM pipeline combines a learning-based odometry module with monocular thermal depth estimation and a dense mapping module powered by 3D Gaussian Splatting. The odometry subsystem enhances tracking robustness on low-texture thermal data, while the mapping subsystem constructs a dense 3D Gaussian representation supervised by selected keyframes and refined depth predictions. To adapt learning-based components to thermal imagery, we incorporate dedicated thermal enhancement techniques for converting 16-bit thermal inputs to 8-bit representations suitable for learning-based modules. The proposed system is evaluated on two thermal SLAM benchmarks—RRXIO[40] and VIVID[41]—and achieves superior performance in both tracking accuracy and thermal image rendering. Ablation studies further demonstrate the benefits of thermal enhancement and monocular depth prediction.

In summary, our contributions are:

- We present a monocular thermal SLAM system that unifies learning-based odometry, monocular depth priors, thermal enhancement, and Gaussian Splatting for dense mapping.
- By combining monocular depth priors with learning-based odometry and GS, the proposed method achieves state-of-the-art tracking accuracy and rendering quality on thermal SLAM benchmarks.
- We provide extensive evaluation and ablation showing

that with proper enhancement, learning-based VO and mapping can transfer effectively to thermal imagery and enable accurate dense reconstruction in challenging illumination conditions.

II. METHOD

Given a sequence of monocular thermal infrared images, our objective is to estimate the camera motion (up to scale) and reconstruct the environment using Gaussian Splatting. Because many thermal cameras output 14- or 16-bit images, our pipeline includes a thermal image enhancement module. We do not consider Non-Uniformity Correction (NUC), as the missing or duplicated frames caused by NUC do not affect motion estimation when only image data is used. The proposed learning-based GS SLAM framework for monocular thermal imagery is illustrated in [Fig. 1](#).

For typical thermal inputs such as 14-bit images, we convert them to 8-bit using an adaptive enhancement strategy based on Fieldscale[42]. This conversion allows thermal data to be processed by odometry and mapping networks originally trained on 8-bit images. The effectiveness of Fieldscale compared to other enhancement strategies is validated in the ablation study (Section III.D).

Following the general design of GS-based SLAM systems, the pipeline consists of two modules: a learning-based odometry module and a GS-based mapping module. The odometry module estimates camera motion by combining image information with learned depth priors. The GS mapping module uses the estimated poses, enhanced thermal images, and refined depth predictions to initialize Gaussian primitives and optimize their parameters through combined photometric and geometric losses.

A. Thermal Odometry with Depth Prior

Learning-based visual odometry has demonstrated strong robustness and accuracy across diverse RGB datasets. A representative example is DROID-SLAM, along with several follow-up systems such as GLORIE-SLAM [30]. However, these methods were originally designed for color images and, to our knowledge, have not been validated on thermal camera datasets. To bridge this gap, we adapt and extend DROID-SLAM for thermal infrared sequences. Our main enhancements include the integration of a monocular depth prediction network to support dense depth refinement and a thermal-specific image enhancement module.

The odometry module takes a stream of thermal infrared images as input and estimates both the camera trajectory and a dense 3D structure for keyframes. The Thermal Infrared Odometry (TIO) system is composed of three main components: a recurrent convolutional module, ConvGRU[43], a dense bundle adjustment (DBA) layer[18], and a disparity and scale optimization (DSO) layer[30]. The ConvGRU predicts optical flow updates conditioned on camera poses and dense depth estimates. These dense depths, referred to as DROID depth for clarity, are propagated and refined throughout the pipeline. The DBA layer jointly optimizes camera poses and dense depths using these flow corrections. To improve depth

estimates in low-texture thermal scenes, the system incorporates a pretrained monocular depth prediction network[44]. The DSO layer further refines the dense depth maps and the

affine relationship between the learned monocular depth and the DROID depth.

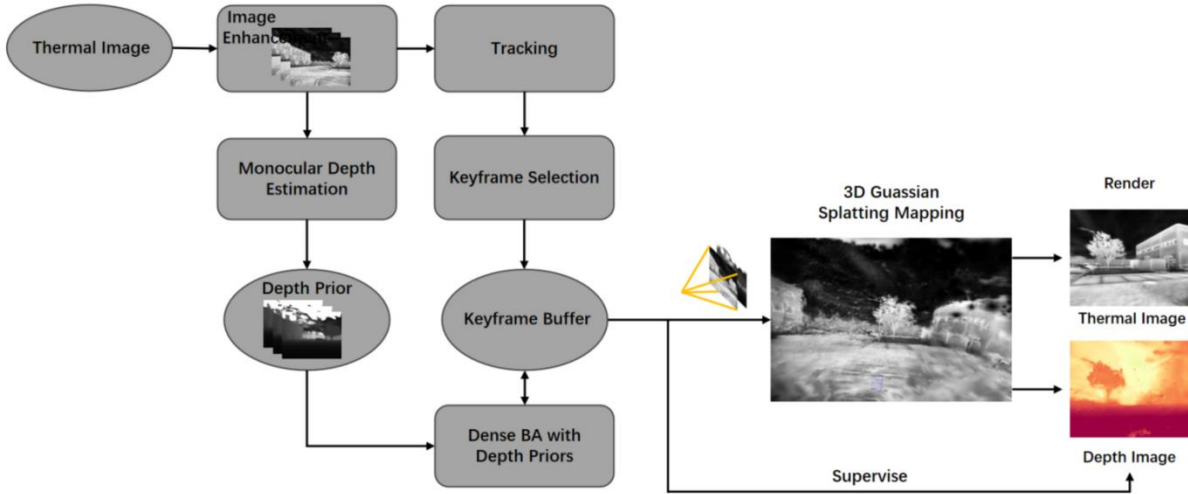


Fig. 1. Overview of the proposed GS-based SLAM system with a learning-based odometry module. Thermal images are first converted from 14- or 16-bit to 8-bit using an image enhancement module. The resulting grayscale images are then processed by a depth prediction network to obtain monocular depth, and simultaneously fed into the learning-based odometry to estimate camera motion. The odometry module tracks each frame against selected keyframes, performs keyframe selection, and refines keyframe poses and dense depth maps by fusing learned depth priors. The refined keyframes and depth estimates are finally passed to the 3D GS mapping module, which optimizes the 3D Gaussians representing the scene.

To represent the trajectory and map, TIO maintains a co-visibility graph $G(V, E)$ for keyframes. Keyframes are selected based on the magnitude of optical flow between frames. Each vertex V_i corresponds to a keyframe I_i and stores its pose \mathbf{T}_i in a world frame and its dense inverse depth map d_i . An edge $(i, j) \in E$ indicates that frames I_i and I_j have an overlapping view. Pixel coordinates $\mathbf{p}_i \in R^{H \times W \times 2}$ in I_i are projected into I_j to obtain \mathbf{p}_{ij} as defined by:

$$\mathbf{p}_{ij} = \Pi(\mathbf{T}_{ij}\Pi^{-1}(\mathbf{p}_i, d_i)), \mathbf{T}_{ij} = \mathbf{T}_j^{-1}\mathbf{T}_i \quad (1)$$

where Π is the projection function that maps 3D points to image coordinates. Its inverse, Π^{-1} , back-projects pixel coordinates \mathbf{p}_i with inverse depths d_i into 3D.

The graph update operation consists of two stages: the convolutional GRU predicts optical-flow corrections for pixel correspondences, and the DBA module refines camera poses and depths using the predicted flow.

For each frame, TIO extracts correlation and context features using two residual blocks. The correlation features capture visual similarity between pixels in images I_i and I_j , while the context features help reject incorrect correspondences arising from dynamic regions or large moving objects. For each edge (i, j) , the convolutional GRU takes the correlation features and the flow residuals $\mathbf{p}_{ij} - \mathbf{p}_i$ to estimate a flow correction $\mathbf{r}_{ij} \in R^{H \times W \times 2}$ and a confidence map $\mathbf{w}_{ij} \in R^{H \times W \times 2}$. The DBA then refines both camera poses and dense

depths over the co-visibility graph using the classic reprojection error objective

$$L(\mathbf{T}, d) = \sum_{i,j} \left\| \mathbf{p}_{ij} + \mathbf{r}_{ij} - \Pi(\mathbf{T}_{ij} \cdot \Pi^{-1}(\mathbf{p}_i, d_i)) \right\|_{\Sigma_{ij}}^2 \quad (2)$$

$$\Sigma_{ij} = \text{diag}(\mathbf{w}_{ij})$$

where $\|\cdot\|_{\Sigma}$ denotes the Mahalanobis distance. To limit computational complexity, older edges are gradually pruned from the graph. The first camera pose is fixed to eliminate gauge freedom.

For each incoming frame, TIO initializes its pose via a linear motion model and propagates inverse depths from the previous frame. The current frame is connected to its three nearest keyframes, and an update step is performed to estimate optical flow and refine its pose, effectively tracking the current frame. A new keyframe is created whenever the mean optical flow relative to last keyframe exceeds a threshold τ .

To complement the often sparse DROID depth estimates, the DSO component fuses them with depth predictions from a pretrained depth network such as Depth Anything[45], ZoeDepth[46] or Metric3D[44]. Depth Anything, based on Dense Vision Transformers (DPTs)[47], predicts per-pixel relative depth, whereas ZoeDepth and Metric3D provides per-pixel metric depth. However, due to scale ambiguity in monocular visual SLAM, the depth scale predicted by these networks typically differs from that of the DROID depth.

To reconcile these depth estimates, DSO optimizes both the high-error depth pixels and the affine transformation between monocular and DROID depth maps. Given a DROID depth

map $D_i = 1/d_i$ for I_i , high-error pixels d_i^h are identified by evaluating multi-view consistency. If the world coordinates derived from each keyframe for a given pixel differ by less than $\eta \cdot \text{avg}(D_i)$, the pixel is considered low-error; otherwise, it is marked as high-error. Formally, $d_i = \{d_i^l, d_i^h\}$. DSO then jointly optimizes keyframe depths and the affine scale and shift θ_i, γ_i that align the monocular prediction D_i^{mono} with the DROID prediction D_i with the objective

$$\begin{aligned} L(d^h, \theta, \gamma) = & \sum_{(i,j) \in E} \left\| \mathbf{p}_{ij} + \mathbf{r}_{ij} - \Pi \left(\mathbf{T}_{ij} \Pi^{-1}(\mathbf{p}_i, d_i) \right) \right\|_{\Sigma_{ij}}^2 \\ & + \alpha_1 \sum_{i \in V} \|d_i^h - (\theta_i/D_i^{mono} + \gamma_i)\|^2 \\ & + \alpha_2 \sum_{i \in V} \|d_i^l - (\theta_i/D_i^{mono} + \gamma_i)\|^2 \end{aligned} \quad (3)$$

where $\alpha_1=0.01$ and $\alpha_2=0.1$ balance the refinement of the depth scale and shift based on low-error pixels, and the refinement of depths for high-error pixels. The affine parameters are initialized for each frame I_i using a least-squares estimation

$$L(\theta_i, \gamma_i) = \|d_i^l - (\theta_i/D_i^{mono} + \gamma_i)\|^2 \quad (4)$$

In optimization, DBA and DSO alternates a few times to improve overall accuracy.

B. Dense Mapping via Gaussian Splatting

Given the estimated camera poses and the dense depth maps of keyframes, the mapping module constructs a scene representation using Gaussian Splatting. To improve efficiency and reduce redundancy, keyframes are further filtered using the co-visibility criteria from MonoGS. Although GS supports pose refinement during mapping, we disable this option to avoid introducing inconsistencies with the odometry poses.

The scene is represented as a collection of 3D Gaussians. Each Gaussian G_i is characterized by its color c_i , opacity $o_i \in R^1$, center position $\mathbf{\mu}_i \in R^3$, and a scaling vector $s_i \in R^3$. For simplicity, the spherical harmonics for view-dependent color computation is omitted and directly use grayscale intensity as the Gaussian color c_i . The rotation matrix \mathbf{R}_i and the scaling matrix $\mathbf{S}_i = \text{diag}(s_1, s_2, s_3)$ together define the covariance of a Gaussian G_i as $\Sigma_{W,i} = \mathbf{R}_i \mathbf{S}_i (\mathbf{R}_i \mathbf{S}_i)^T$. A 3D Gaussian influences a point $\mathbf{x} \in R^3$ according to

$$G_i(\mathbf{x}) = o_i \exp[-(\mathbf{x} - \mathbf{\mu}_i)^T \Sigma_{W,i}^{-1} (\mathbf{x} - \mathbf{\mu}_i)] \quad (5)$$

To render an image from a set of Gaussians, we first sort the Gaussians by their center depth. Each 3D Gaussian is then projected onto the image plane, forming a 2D Gaussian G'_i with image-plane center $\mathbf{\mu}'_i$ and covariance Σ'_i

$$\mathbf{\mu}'_i = \pi(\mathbf{T}_{CW} \cdot \mathbf{\mu}_i) \quad (6)$$

$$\Sigma'_i = \mathbf{J} \mathbf{R}_{CW} \Sigma_{W,i} \mathbf{R}_{CW}^T \mathbf{J}^T \quad (7)$$

where $\mathbf{J} = \frac{\partial \pi(\mathbf{p}_c)}{\partial \mathbf{p}_c}$ is the Jacobian of the projection and \mathbf{T}_{CW} transforms world coordinates into the camera frame. The projection π is defined by

$$\mathbf{W} = \mathbf{T}_{ndc}^{pix} \cdot \mathbf{T}_{cam}^{ndc} \quad (8)$$

where \mathbf{T}_{cam}^{ndc} maps camera coordinates to normalized device coordinates (NDC), and \mathbf{T}_{ndc}^{pix} map NDC to pixel coordinates.

The 2D Gaussian G'_i contributes to a pixel $\mathbf{x}' \in R^2$ as

$$G'_i(\mathbf{x}') = o_i \exp[-(\mathbf{x}' - \mathbf{\mu}'_i)^T \Sigma'_i^{-1} (\mathbf{x}' - \mathbf{\mu}'_i)] \quad (9)$$

To compute the final pixel intensity at $\mathbf{p} = (u, v)$, all n Gaussians sorted by are composited front-to-back using volumetric alpha blending:

$$c(\mathbf{p}) = \sum_{i=1}^n c_i G'_i(\mathbf{p}) \prod_{j=1}^{i-1} (1 - G'_j(\mathbf{p})) \quad (10)$$

In practice, the image is partitioned into 16×16 tiles. For each tile, we identify all projected 2D Gaussians whose centers fall inside the tile and then perform alpha blending using only the Gaussians intersecting the tile.

Depth rendering follows the same formulation. To get the depth of a pixel, $D(\mathbf{x})$, we simply replace c_i by the 2D Gaussian's depth $z_i = [\mathbf{R}_{CW} \mathbf{\mu}_i + \mathbf{p}_{CW}]_z$.

During training, the gray images and proxy depths from the odometry module supervise the learnable GS parameters. The overall loss function comprises a color loss L_c , a structural similarity loss L_{SSIM} , and a depth loss L_d ,

$$L = (1 - \alpha)L_c + \alpha L_{SSIM} + \beta L_d \quad (11)$$

with empirical weights $\alpha = 0.2$ and $\beta = 0.2$. The terms L_c and L_{SSIM} measure the photometric and structural differences between rendered and observed images, while L_d is the mean L_1 difference between the rendered depth and the proxy depth.

To better condition GS mapping, we adopt the common strategy used in Splat-SLAM and supervise the GS depth using a proxy depth. The proxy depth is computed by fusing the DROID depth estimates \widehat{D} with monocular depth predictions D^{mono} . For each frame I_i , the scale and shift of the monocular depth are estimated using a least squares approach with the following objective:

$$L(\theta'_i, \gamma'_i) = \|\widehat{D}_i - (\theta'_i D_i^{mono} + \gamma'_i)\|^2 \quad (12)$$

The resulting the proxy (inverse) depth D_i^p is given by:

$$D_i^p = \begin{cases} \widehat{D}_i(u, v), & \text{if } \widehat{D}_i(u, v) \text{ is low error} \\ \theta'_i D_i^{mono}(u, v) + \gamma'_i & \text{otherwise} \end{cases} \quad (13)$$

With the proxy depth, for each keyframe, Gaussians are

spawned by sampling depths from the proxy frame. For Gaussian densification, the AbsGS strategy[34] is adopted to insert new Gaussians based on the magnitude of the gradient with respect to the 2D Gaussian positions. While the absolute gradient guides densification, the signed gradient is retained for backpropagation. To prune redundant Gaussians, those Gaussians with low opacity and large spatial extent are removed following the approach used in MonoGS and SplatTAM. Specifically, Gaussians with opacity below a threshold of 0.05 are removed. In addition, newly generated Gaussians that are not observed in at least three previous frames are also discarded.

III. EXPERIMENTS

We evaluate the proposed monocular thermal odometry and Gaussian Splatting-based mapping framework (TOM-GS) on two public benchmarks, RRXIO[40] and VIVID[41], focusing on both tracking accuracy and reconstruction quality.

The RRXIO dataset contains nine sequences captured in indoor and outdoor scenes using a monochrome camera (1280×1024) and a thermal camera (640×512). Indoor sequences include accurate ground truth from a motion capture system, while outdoor reference trajectories are generated using visual-inertial SLAM. During preprocessing, grayscale images from both cameras are converted to three channels and undistorted. The VIVID dataset contains 14 sequences covering indoor and outdoor environments. It includes RGB-D data (640×480) and thermal images captured with a FLIR A65 camera (640×512). Since VIVID thermal data are provided in 14-bit format, the image enhancement module in Fig. 1 is required before feeding the images to odometry and mapping networks.

We evaluate camera tracking using the absolute trajectory error (ATE) Root Mean Square Error (RMSE) [48] computed after aligning the estimated trajectory to the reference using a Sim(3) transformation. Image rendering performance is evaluated using PSNR (Peak Signal-to-Noise Ratio), SSIM (Structural Similarity Index Measure), and LPIPS (Learned Perceptual Image Patch Similarity) [35].

For comparison, we choose several recent monocular SLAM baselines, including classical geometric methods

(ORB-SLAM3[5], LDSO[49]), learning-based odometry (DROID-SLAM[18], DPVO [26], ThermalMonoDepth[19]), NeRF-based mapping approaches (NeRF-VO[31], GLORIE-SLAM[30]), and GS-based methods (MonoGS[35], PhotoSLAM[37]).

A. Odometry Evaluation

For motion tracking, we compare ORB-SLAM3, LDSO, DROID-SLAM, DPVO, NeRF-VO, GLORIE-SLAM, MonoGS, ThermalMonoDepth, and TOM-GS on the RRXIO dataset. We keep the image resolution at 640×512 for ORB-SLAM3 and LDSO. For other methods, we resize the images to 320×256 to reduce GPU memory use. NeRF-VO, GLORIE-SLAM, MonoGS, and PhotoSLAM are run in sequential mode. We keep the global BA module enabled for DROID-SLAM, GLORIE-SLAM, and loop closure enabled for ORB-SLAM3, LDSO, and PhotoSLAM.

Table I reports the ATE for visual and thermal inputs on RRXIO. As expected, odometry accuracy with coarse thermal images is generally lower than with visual images under well-lit conditions, but surpasses visual performance in challenging settings such as low-light scenes (e.g., mocap_dark). Geometric methods often fail on thermal sequences. DROID-SLAM remains competitive, but our method boosted by depth priors outperforms it in many cases.

For the VIVID dataset, TABLE II shows ATE results for RGB images and for thermal images enhanced with Fieldscale. Learning-based methods significantly outperform geometric methods across most sequences. Importantly, odometry performance using thermal data is generally superior to that using RGB, reflecting the robustness of thermal imaging under variable illumination. Our method achieves leading performance among the learning-based approaches.

Table I ABSOLUTE TRANSLATION ERROR (ATE) RMSE (VISUAL | THERMAL) OF MONOCULAR ODOMETRY METHODS ON RRXIO. ORB3, DROID, PHOTO, AND GLORIE REFER TO ORB-SLAM3, DROID-SLAM, PHOTOSLAM, AND GLORIE-SLAM, RESPECTIVELY, AND TMD DENOTES THERMALMONODEPTH. ‘-’ INDICATES TRACKING FAILURE. **BEST** IS BOLDED; SECOND-BEST IS UNDERLINED (VISUAL/THERMAL, RESPECTIVELY).

| Sed | ORB3 | LDSO | DROID | DPVO | NeRFVO | TMD | Photo | MonoGS | GLORIE | Ours |
|-----------------|--------------------|-------------|---------------------------|---------------------------|--------------------|--------------------|---------------------------|-------------|---------------------------|---------------------------|
| mocap_easy | 0.02 0.16 | 0.03 1.12 | 0.02 0.02 | 0.11 0.24 | 0.13 0.24 | 1.53 1.54 | 0.02 1.04 | 1.57 1.64 | 0.02 <u>0.03</u> | 0.02 0.02 |
| mocap_medium | 0.06 0.34 | 0.64 - | 0.06 0.07 | 0.16 0.52 | - 0.81 | 1.44 1.45 | 0.06 0.86 | 1.48 - | 0.06 0.07 | 0.06 0.07 |
| mocap_difficult | - - | 1.40 - | 0.02 1.39 | <u>0.16</u> <u>1.12</u> | - 6.19 | 1.56 1.57 | 1.34 - | 1.58 - | - - | 0.02 0.07 |
| mocap_dark | - <u>0.11</u> | - 1.41 | 1.53 0.08 | <u>1.54</u> 1.29 | - 0.47 | <u>1.54</u> 1.54 | - 1.18 | - 1.58 | <u>1.54</u> - | 1.55 0.08 |
| mocap_dark_fast | - 0.17 | - - | <u>1.41</u> 0.04 | 1.40 0.21 | - 0.34 | 1.40 1.41 | - 0.86 | - - | 1.46 <u>0.06</u> | 1.47 <u>0.06</u> |
| indoor_floor | 2.64 0.25 | 5.08 - | <u>0.33</u> <u>6.14</u> | 1.03 9.72 | 9.27 12.60 | 10.44 10.45 | 5.62 10.51 | 3.65 - | - - | 0.17 9.66 |
| gym | 0.05 2.46 | 0.15 - | 0.03 0.29 | 0.37 5.50 | - <u>0.92</u> | 5.46 5.46 | 0.36 3.49 | 4.82 5.12 | 2.11 1.02 | 2.11 1.02 |
| outdoor_street | 0.33 - | 0.39 - | 0.15 4.00 | 0.61 0.90 | - - | 8.57 19.23 | <u>0.18</u> 0.15 | - - | 0.19 <u>0.35</u> | 0.21 0.43 |
| outdoor_campus | 0.22 0.14 | 0.28 0.27 | 0.13 <u>0.16</u> | 0.19 0.18 | <u>0.14</u> 0.24 | 10.93 13.65 | 0.24 0.45 | - - | 0.15 0.23 | 0.15 0.22 |
| Mean | 0.56 0.51 | 1.14 0.93 | <u>0.41</u> 1.35 | 0.62 2.19 | 3.18 2.72 | 4.76 6.26 | 1.12 2.32 | 2.62 2.78 | 0.62 0.19 | 0.23 <u>0.35</u> |

TABLE II ABSOLUTE TRANSLATION ERROR (ATE) RMSE (VISUAL | THERMAL) OF MONOCULAR VISUAL ODOMETRY METHODS ON VIVID. THE DATASET INCLUDES INDOOR (IN) AND OUTDOOR (OUT) SEQUENCES, WITH SLOW (ROB), UNSTABLE (UNST), AND AGGRESSIVE (AGG) MOTION UNDER VARIOUS LIGHTING CONDITIONS: LIGHTS ON (GLOBAL), LIGHTS OFF (DARK), FLASHLIGHT (LOCAL), AND FLASHLIGHT GRADUALLY TRANSITIONING FROM DARK TO LOCAL (VARYING). ORB3, DROID, PHOTO, AND GLORIE CORRESPOND TO ORB-SLAM3, DROID-SLAM, PHOTOSLAM, AND GLORIESLAM, RESPECTIVELY, AND TMD DENOTES THERMALMONODEPTH. ‘-’ INDICATES TRACKING FAILURE. **BEST** IS BOLDED; **SECOND-BEST** IS UNDERLINED (VISUAL/THERMAL, RESPECTIVELY).

| Seq | ORB3 | LDSO | DROID | DPVO | NeRFVO | TMD | Photo | MonoGS | GLORIE | Ours |
|----------------|--------------------|--------------------|---------------------------|--------------------|---------------------------|-------------|---------------------------|--------------|---------------------------|---------------------------|
| in rob_global | 0.08 - | 0.52 - | <u>0.09</u> 0.67 | 0.09 0.51 | 0.08 0.18 | 0.66 0.27 | 0.46 - | 0.58 0.69 | <u>0.09</u> 0.08 | 0.09 0.07 |
| in unst_global | 0.04 - | - - | 0.06 0.08 | 0.25 0.67 | 0.12 2.71 | 0.80 0.54 | 0.51 - | 0.76 - | 0.06 <u>0.31</u> | 0.06 0.33 |
| in agg_global | 0.08 - | - - | 0.46 0.08 | 0.17 0.76 | 0.16 1.81 | 0.78 0.65 | - - | 0.69 0.75 | 0.11 0.08 | - 0.09 |
| in rob_dark | - 0.04 | - 0.45 | 0.52 0.06 | 0.49 0.14 | 0.78 0.05 | 0.51 0.42 | - 0.29 | - 0.48 | 0.43 0.07 | 0.48 0.05 |
| in unst_dark | - - | - - | <u>0.64</u> 0.06 | 0.62 0.19 | 0.94 0.09 | 0.75 0.38 | - - | - 0.72 | 0.71 0.06 | 0.72 0.06 |
| in agg_dark | - - | - - | 0.64 0.09 | 0.69 0.61 | 1.66 0.10 | 0.70 0.70 | - - | - - | 0.69 0.09 | 0.66 0.63 |
| in rob_local | 0.32 - | <u>0.23</u> 0.51 | 0.06 0.05 | 0.06 0.07 | 0.06 0.05 | 0.42 0.29 | 0.06 - | 0.41 0.35 | 0.06 0.06 | 0.06 0.06 |
| in unst_local | - - | 0.65 0.69 | 0.04 0.04 | 0.09 0.09 | 0.04 0.05 | 0.67 0.38 | 0.24 - | 0.63 0.52 | 0.04 0.04 | 0.04 0.04 |
| in agg_local | 0.07 - | - - | 0.11 0.07 | 0.24 <u>0.16</u> | 0.16 0.09 | 0.61 0.60 | 0.25 - | 0.53 - | 0.11 0.56 | - 0.51 |
| in rob_varying | 0.18 0.04 | - - | 0.55 0.03 | 0.12 0.07 | 4.44 0.04 | 0.55 0.46 | 0.51 0.20 | 0.49 0.31 | 0.07 0.03 | 0.06 0.03 |
| out rob_day1 | - - | - - | 0.36 5.91 | 0.54 0.83 | 0.74 1.75 | 1.73 1.74 | 0.36 0.41 | 10.31 6.13 | 0.37 1.25 | 0.37 1.24 |
| out rob_day2 | - - | - - | 0.25 1.94 | 0.29 1.36 | 0.37 1.81 | 2.97 2.98 | 0.76 1.46 | 7.93 7.55 | 0.25 0.24 | 0.26 0.24 |
| out rob_night1 | - - | 10.91 - | 2.38 3.20 | 4.32 1.24 | 0.73 <u>1.16</u> | 3.05 3.05 | 11.51 0.96 | - 5.29 | 2.02 1.97 | 1.97 2.06 |
| out rob_night2 | 0.85 1.20 | - - | 6.66 0.24 | 1.08 0.95 | 0.38 1.33 | 2.56 2.56 | 10.44 1.31 | - 6.61 | 0.28 0.28 | 0.40 0.29 |
| Mean | 0.23 0.43 | 3.08 0.55 | 0.92 0.89 | 0.65 0.55 | 0.76 0.80 | 1.20 1.07 | 2.51 0.77 | 2.48 2.67 | 0.38 0.37 | 0.37 0.41 |

B. Visual Rendering Evaluation

For visual rendering, we compare dense reconstruction methods including NeRF-VO, GLORIE-SLAM, MonoGS, PhotoSLAM, and our TOM-GS. For evaluation, we sample every fifth frame from each sequence, excluding those used for GS or NeRF training. All methods are tested on both the RRXIO and VIVID datasets. We report SSIM, LPIPS, and PSNR to quantify rendering quality. The rendering metrics for the RRXIO sequences are summarized in **TABLE III**. Overall,

GS-based mapping with thermal inputs achieves better rendering quality than with monochrome visual data, especially on dark sequences where thermal imaging is more informative. Our GS-based mapping method attains leading performance on most sequences. However, in large-scale scenes, our method occasionally fails due to GPU memory exhaustion, even on an RTX 4090, and such failed cases are excluded from the averages.

TABLE III RENDERING RESULTS ON THE RRXIO SEQUENCES USING NERF-VO, PHOTOSLAM, MONOGS, GLORIE-SLAM, AND OUR TOM-GS. PHOTO AND GLORIE DENOTE PHOTOSLAM AND GLORIE-SLAM, RESPECTIVELY. ‘-’ INDICATES FAILURE. AVERAGE VALUES ARE COMPUTED OVER SUCCESSFUL RUNS. **BEST** IS BOLDED; **SECOND-BEST** IS UNDERLINED.

| Method | Metric | easy | medium | diff. | dark | fast | floor | gym | street | campus | Avg. |
|----------------|--------|-------|--------|-------|-------|-------|-------|-------|--------|--------|--------------|
| NeRFVO+Gray | PSNR↑ | 28.27 | - | - | - | - | 27.97 | - | - | 29.23 | 28.49 |
| | SSIM↑ | 0.16 | - | - | - | - | 0.06 | - | - | 0.36 | 0.19 |
| | LPIPS↓ | 0.60 | - | - | - | - | 0.80 | - | - | 0.47 | 0.62 |
| NeRFVO+Thermal | PSNR↑ | 28.55 | 28.28 | 28.25 | 28.19 | 28.29 | 28.02 | 28.36 | - | 29.36 | 28.41 |
| | SSIM↑ | 0.23 | 0.13 | 0.17 | 0.15 | 0.21 | 0.01 | 0.14 | - | 0.39 | 0.18 |
| | LPIPS↓ | 0.61 | 0.65 | 0.56 | 0.65 | 0.62 | 0.64 | 0.65 | - | 0.44 | 0.60 |
| Photo+Gray | PSNR↑ | 26.83 | 26.62 | 16.73 | - | - | 18.90 | 24.34 | 19.90 | 25.98 | 22.76 |
| | SSIM↑ | 0.89 | 0.90 | 0.72 | - | - | 0.79 | 0.80 | 0.72 | 0.78 | 0.80 |
| Photo+Thermal | PSNR↑ | 27.03 | 29.97 | - | 24.59 | 32.83 | 24.79 | 29.93 | 24.02 | 27.93 | 27.64 |
| | SSIM↑ | 0.86 | 0.87 | - | 0.83 | 0.90 | 0.86 | 0.89 | 0.77 | 0.86 | 0.86 |
| MonoGS+Gray | PSNR↑ | 17.16 | 17.65 | 14.25 | - | - | 7.21 | 20.75 | - | - | 15.40 |
| | SSIM↑ | 0.69 | 0.70 | 0.59 | - | - | 0.33 | 0.70 | - | - | 0.60 |
| | LPIPS↓ | 0.60 | 0.57 | 0.64 | - | - | 0.81 | 0.45 | - | - | 0.61 |
| MonoGS+Thermal | PSNR↑ | 23.50 | - | - | 15.40 | - | - | 25.84 | - | - | 21.58 |
| | SSIM↑ | 0.82 | - | - | 0.40 | - | - | 0.85 | - | - | 0.69 |
| | LPIPS↓ | 0.62 | - | - | 0.82 | - | - | 0.58 | - | - | 0.67 |
| GLORIE+Gray | PSNR↑ | 17.87 | 17.83 | - | 31.21 | 31.18 | - | 19.86 | 13.80 | 18.36 | 21.45 |
| | SSIM↑ | 0.72 | 0.69 | - | 0.80 | 0.81 | - | 0.74 | 0.54 | 0.68 | 0.71 |
| | LPIPS↓ | 0.62 | 0.64 | - | 0.08 | 0.07 | - | 0.60 | 0.77 | 0.59 | 0.48 |
| GLORIE+Thermal | PSNR↑ | 23.77 | 21.67 | - | - | 22.61 | - | 21.16 | 18.91 | 22.59 | 21.78 |
| | SSIM↑ | 0.77 | 0.67 | - | - | 0.72 | - | 0.65 | 0.63 | 0.74 | 0.69 |
| | LPIPS↓ | 0.50 | 0.57 | - | - | 0.54 | - | 0.65 | 0.61 | 0.54 | 0.57 |
| Ours+Gray | PSNR↑ | 28.55 | 27.08 | 26.34 | - | - | 28.23 | - | - | - | 27.55 |
| | SSIM↑ | 1.00 | 1.00 | 1.00 | - | - | 1.00 | - | - | - | 1.00 |
| | LPIPS↓ | 0.07 | 0.10 | 0.10 | - | - | 0.10 | - | - | - | 0.09 |
| Ours+Thermal | PSNR↑ | 30.76 | 27.90 | 25.63 | 28.33 | 28.46 | - | 33.00 | - | - | 29.01 |
| | SSIM↑ | 1.00 | 1.00 | 1.00 | 1.00 | 1.00 | - | 1.00 | - | - | 1.00 |
| | LPIPS↓ | 0.22 | 0.29 | 0.42 | 0.27 | 0.30 | - | 0.25 | - | - | 0.29 |

The rendering results on the VIVID dataset are reported in **TABLE IV**. For well-illuminated sequences, such as outdoor_robust_day1, RGB-based rendering typically outperforms thermal rendering, reflecting the richer texture and color

information. Under low-light or challenging illumination, however, RGB-based methods degrade significantly, whereas thermal-based rendering remains stable. With proxy-depth-supervised GS training, our method achieves

leading thermal rendering quality among all compared approaches. Overall, rendering quality on thermal data is more consistent across illumination conditions than on RGB data,

and more RGB sequences fail and are therefore omitted from the metric computation.

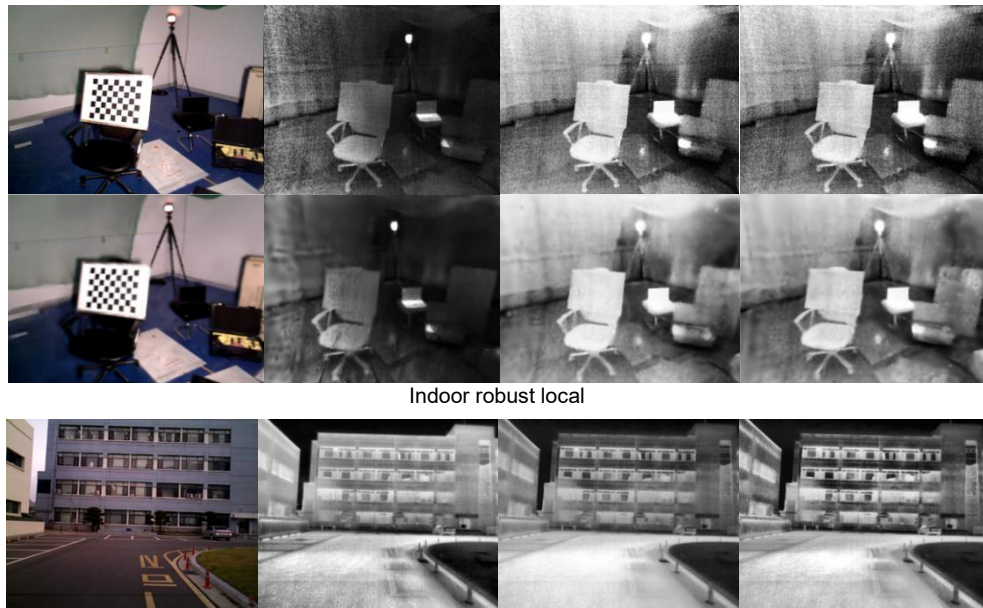
TABLE IV RENDERING COMPARISONS ON VIVID SEQUENCES USING NERF-VO, PHOTOSLAM, MONOGS, GLORIE-SLAM, AND OUR TOM-GS. THE DATASET INCLUDES INDOOR (IN) AND OUTDOOR (OUT) SEQUENCES, WITH SLOW (ROB), UNSTABLE (UNST), AND AGGRESSIVE (AGG) MOTION UNDER VARIOUS ILLUMINATION CONDITIONS: LIGHTS ON (GLOBAL), LIGHTS OFF (DARK AND NIGHT), FLASHLIGHT (LOCAL), AND FLASHLIGHT GRADUALLY TRANSITIONING FROM DARK TO LOCAL (VARYING). **BEST** IS BOLDED; SECOND-BEST IS UNDERLINED.

| Method | Metric | IRG | IUG | IAG | IRD | IUD | IAD | IRL | IUL | IAL | IRV | ORD1 | ORD2 | ORN1 | ORN2 | Avg. | |
|----------------|--------------------|-------|-------|-------|-------|-------|-------|-------|-------|-------|-------|-------|-------|-------|-------|--------------|------|
| NeRFVO+RGB | PSNR \uparrow | 28.03 | 27.93 | 28.04 | - | - | - | 28.18 | 28.31 | 28.17 | 28.31 | 28.13 | 28.02 | - | - | 28.12 | |
| | SSIM \uparrow | 0.21 | 0.20 | 0.19 | - | - | - | 0.17 | 0.18 | 0.19 | 0.28 | 0.28 | 0.26 | - | - | 0.22 | |
| | LPIPS \downarrow | 0.62 | 0.65 | 0.65 | - | - | - | 0.55 | 0.55 | 0.56 | 0.52 | 0.56 | 0.56 | - | - | 0.58 | |
| NeRFVO+Thermal | PSNR \uparrow | 28.03 | 28.00 | 27.72 | 27.59 | 28.63 | 27.61 | 27.93 | 27.67 | 27.91 | 27.68 | 28.00 | 28.00 | 28.09 | 28.10 | 27.93 | |
| | SSIM \uparrow | 0.34 | 0.24 | 0.28 | 0.27 | 0.44 | 0.32 | 0.51 | 0.48 | 0.41 | 0.44 | 0.09 | 0.10 | 0.10 | 0.13 | 0.30 | |
| | LPIPS \downarrow | 0.36 | 0.39 | 0.35 | 0.43 | 0.28 | 0.39 | 0.25 | 0.27 | 0.30 | 0.30 | 0.67 | 0.66 | 0.63 | 0.58 | <u>0.42</u> | |
| Photo+RGB | PSNR \uparrow | 17.23 | 14.43 | 18.96 | - | - | - | 20.07 | 19.61 | 24.51 | 15.90 | 20.50 | 20.76 | 22.39 | 21.61 | 19.64 | |
| | SSIM \uparrow | 0.62 | 0.55 | 0.70 | - | - | - | 0.67 | 0.67 | 0.71 | 0.52 | 0.68 | 0.68 | 0.88 | 0.90 | 0.69 | |
| Photo+Thermal | PSNR \uparrow | - | - | - | 24.74 | - | - | 25.93 | - | - | 25.11 | 20.09 | 19.66 | 25.13 | 24.43 | 23.58 | |
| | SSIM \uparrow | - | - | - | 0.79 | - | - | 0.81 | - | - | 0.83 | 0.63 | 0.63 | 0.75 | 0.74 | <u>0.74</u> | |
| MonoGS+RGB | PSNR \uparrow | 17.18 | 17.25 | 15.51 | - | - | - | 19.12 | 17.58 | 16.38 | 13.11 | 21.48 | 22.23 | - | - | 17.76 | |
| | SSIM \uparrow | 0.60 | 0.62 | 0.56 | - | - | - | 0.61 | 0.57 | 0.52 | 0.47 | 0.68 | 0.72 | - | - | 0.59 | |
| | LPIPS \downarrow | 0.47 | 0.53 | 0.59 | - | - | - | 0.47 | 0.56 | 0.65 | 0.63 | 0.43 | 0.35 | - | - | 0.52 | |
| MonoGS+Thermal | PSNR \uparrow | 24.13 | - | 20.53 | 24.00 | 22.08 | - | 26.22 | 24.05 | - | 23.89 | 22.60 | 23.47 | 22.09 | 22.31 | 23.22 | |
| | SSIM \uparrow | 0.64 | - | 0.55 | 0.72 | 0.67 | - | 0.76 | 0.72 | - | 0.74 | 0.67 | 0.71 | 0.67 | 0.69 | 0.69 | |
| | LPIPS \downarrow | 0.60 | - | 0.74 | 0.55 | 0.63 | - | 0.49 | 0.54 | - | 0.52 | 0.48 | 0.43 | 0.48 | 0.50 | 0.54 | |
| GLORIE+RGB | PSNR \uparrow | 16.04 | 15.66 | 15.19 | 40.32 | 40.17 | 36.37 | 17.84 | 18.06 | 17.07 | 13.77 | 15.68 | 17.27 | 18.79 | 19.06 | 21.52 | |
| | SSIM \uparrow | 0.70 | 0.61 | 0.59 | 0.98 | 0.98 | 0.97 | 0.72 | 0.73 | 0.62 | 0.34 | 0.64 | 0.67 | 0.69 | 0.69 | <u>0.71</u> | |
| | LPIPS \downarrow | 0.53 | 0.66 | 0.70 | 0.09 | 0.09 | 0.10 | 0.52 | 0.56 | 0.65 | 0.75 | 0.63 | 0.63 | 0.39 | 0.39 | <u>0.48</u> | |
| GLORIE+Thermal | PSNR \uparrow | 21.39 | 20.12 | 20.45 | 22.06 | 20.75 | 21.59 | 22.64 | 23.13 | 22.13 | 24.06 | - | - | - | 17.18 | 21.08 | |
| | SSIM \uparrow | 0.71 | 0.63 | 0.64 | 0.78 | 0.72 | 0.73 | 0.80 | 0.80 | 0.75 | 0.81 | - | - | - | 0.66 | 0.67 | 0.72 |
| | LPIPS \downarrow | 0.51 | 0.55 | 0.55 | 0.46 | 0.50 | 0.50 | 0.43 | 0.43 | 0.50 | 0.42 | - | - | - | 0.61 | 0.60 | 0.50 |
| Ours+RGB | PSNR \uparrow | 18.10 | 21.85 | 22.00 | 20.13 | 23.74 | 24.86 | 18.49 | 21.89 | 23.51 | 17.38 | 24.94 | 25.60 | 23.72 | 23.41 | 22.12 | |
| | SSIM \uparrow | 1.00 | 1.00 | 1.00 | 1.00 | 1.00 | 1.00 | 1.00 | 1.00 | 1.00 | 1.00 | 1.00 | 1.00 | 1.00 | 1.00 | 1.00 | |
| | LPIPS \downarrow | 0.07 | 0.26 | 0.32 | 0.09 | 0.10 | 0.13 | 0.09 | 0.23 | 0.19 | 0.31 | 0.12 | 0.10 | 0.09 | 0.07 | <u>0.16</u> | |
| Our+Thermal | PSNR \uparrow | 27.28 | 26.20 | 27.98 | 28.73 | 27.42 | 28.58 | 28.02 | 27.47 | 25.90 | 28.49 | 26.60 | 25.82 | 25.98 | 26.59 | <u>27.22</u> | |
| | SSIM \uparrow | 1.00 | 1.00 | 1.00 | 1.00 | 1.00 | 1.00 | 1.00 | 1.00 | 1.00 | 1.00 | 1.00 | 1.00 | 1.00 | 1.00 | 1.00 | |
| | LPIPS \downarrow | 0.39 | 0.54 | 0.40 | 0.33 | 0.41 | 0.33 | 0.32 | 0.40 | 0.58 | 0.39 | 0.28 | 0.27 | 0.28 | 0.25 | <u>0.37</u> | |

C. Qualitative Evaluation

We further assess the reconstruction quality of TOM-GS on the VIVID dataset through qualitative experiments. For several representative sequences, we visualize both the ground-truth images and the corresponding rendered views. Images in Fig. 2 show that GS can faithfully reproduce fine scene details and

effectively smooth the noise present in the raw thermal images, leading to visually cleaner reconstructions. Also, by comparing the thermal images enhanced by three enhancement methods, Fieldscale, naive, and Shin’s method[19], we see that Fieldscale provides uniformly enhanced images without causing overexposure artifacts.



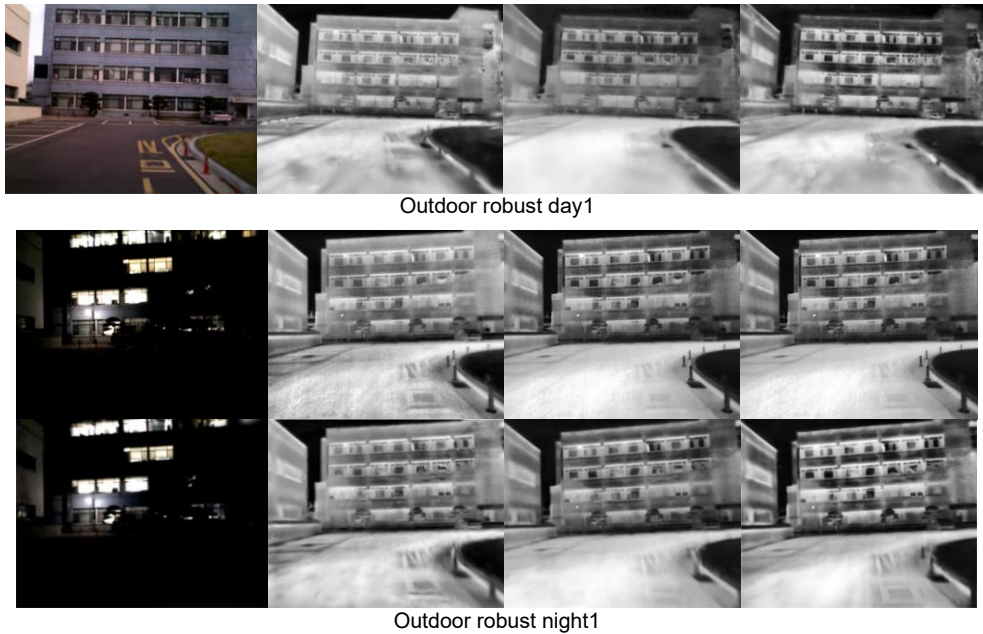


Fig. 2. Rendering results for sampled RGB and thermal images from three VIVID sequences: indoor robust local, outdoor robust day1, outdoor robust night1. In each group, from left to right: RGB, Thermal-Fieldscale, Thermal-naive, and Thermal-Shin; the top row shows the ground truth images, and the bottom row shows the corresponding rendered images.

D. Ablation Study

We conduct a series of ablation studies on the VIVID dataset to analyze the contributions of the depth prior network and the thermal image enhancement module. The evaluated depth-prediction models include Depth Anything, Lotus, Metric3D, and ZoeDepth. The used models are depth-anything-vit14 of 335.3M parameters, lotus-depth-d-v2-0-disparity of 1.29B parameters, metric3d-vit-giant2 of 1.38B parameters, and zoed-M12-NK of 346.1M parameters. For thermal image enhancement, we compare Fieldscale, Shin's method [19], and a naive en-

hancement approach using OpenCV's CLAHE.

TABLE V reports the rendering quality under different combinations of depth priors and enhancement methods. Overall, Metric3D delivers the strongest rendering performance, achieving the best PSNR and LPIPS results, followed by Depth Anything, ZoeDepth, and Lotus. Regarding enhancement methods, FieldScale consistently outperforms Shin's method and the naive baseline, producing higher-quality visual inputs to the learning methods and more stable reconstruction.

TABLE V RENDERING RESULTS OF TOM-GS ON THE VIVID SEQUENCES CONVERTED TO 8BIT USING DIFFERENT ENHANCEMENT METHODS, FIELDSCALE (FS), NAÏVE AND SHIN'S METHOD, AND WITH DIFFERENT DEPTH PRIORS ESTIMATED BY DEPTH ANYTHING (DEPTHANY), LOTUS, METRIC3D, AND ZOEDEPTH. **BEST** IS BOLDED; SECOND-BEST IS UNDERLINE.

| Method | Metric | IAD | IAG | IAL | IRD | IRG | IRL | IRV | IUD | IUG | IUL | ORD1 | ORD2 | ORN1 | ORN2 | Avg. |
|----------------|--------|-------|-------|-------|-------|-------|-------|-------|-------|-------|-------|-------|-------|-------|-------|--------------|
| Depthany-fs | PSNR↑ | 22.38 | 24.66 | 28.30 | 28.24 | 27.29 | 28.34 | 28.31 | 27.37 | 26.47 | 28.51 | 26.32 | 25.21 | 26.30 | 24.62 | 26.59 |
| | SSIM↑ | 1.00 | 1.00 | 1.00 | 1.00 | 1.00 | 1.00 | 1.00 | 1.00 | 1.00 | 1.00 | 1.00 | 1.00 | 1.00 | 1.00 | 1.00 |
| | LPIPS↓ | 0.57 | 0.59 | 0.39 | 0.33 | 0.40 | 0.32 | 0.31 | 0.41 | 0.57 | 0.39 | 0.28 | 0.25 | 0.29 | 0.28 | 0.38 |
| Depthany-naive | PSNR↑ | 22.08 | 25.11 | 19.66 | 21.70 | 26.68 | 20.26 | 20.87 | 20.66 | 26.85 | 21.47 | 28.65 | 28.54 | 29.46 | 26.03 | 24.14 |
| | SSIM↑ | 1.00 | 1.00 | 1.00 | 1.00 | 1.00 | 1.00 | 1.00 | 1.00 | 1.00 | 1.00 | 1.00 | 1.00 | 1.00 | 1.00 | 1.00 |
| | LPIPS↓ | 0.59 | 0.56 | 0.69 | 0.53 | 0.47 | 0.54 | 0.55 | 0.60 | 0.56 | 0.60 | 0.26 | 0.23 | 0.24 | 0.27 | 0.48 |
| Depthany-shin | PSNR↑ | 21.19 | 22.98 | 19.73 | 21.72 | 24.47 | 21.51 | 21.43 | 20.87 | 24.72 | 21.52 | 26.33 | 25.19 | 26.89 | 23.98 | 23.04 |
| | SSIM↑ | 1.00 | 1.00 | 1.00 | 1.00 | 1.00 | 1.00 | 1.00 | 1.00 | 1.00 | 1.00 | 1.00 | 1.00 | 1.00 | 1.00 | 1.00 |
| | LPIPS↓ | 0.53 | 0.64 | 0.69 | 0.51 | 0.55 | 0.51 | 0.51 | 0.57 | 0.66 | 0.60 | 0.30 | 0.24 | 0.29 | 0.30 | 0.49 |
| Lotus-fs | PSNR↑ | 16.83 | 24.80 | 27.60 | 28.62 | 27.36 | 27.59 | 27.95 | 27.10 | 26.56 | 28.72 | 26.05 | 25.31 | 26.31 | 24.31 | 26.08 |
| | SSIM↑ | 0.96 | 1.00 | 1.00 | 1.00 | 1.00 | 1.00 | 1.00 | 1.00 | 1.00 | 1.00 | 1.00 | 1.00 | 1.00 | 1.00 | 1.00 |
| | LPIPS↓ | 0.68 | 0.59 | 0.34 | 0.32 | 0.41 | 0.33 | 0.32 | 0.42 | 0.54 | 0.39 | 0.28 | 0.24 | 0.29 | 0.27 | 0.39 |
| Lotus-naive | PSNR↑ | 22.61 | 26.22 | 20.04 | 21.66 | 26.53 | 20.48 | 20.97 | 21.01 | 27.01 | 21.58 | 28.80 | 26.98 | 29.57 | 24.62 | 24.15 |
| | SSIM↑ | 1.00 | 1.00 | 1.00 | 1.00 | 1.00 | 1.00 | 1.00 | 1.00 | 1.00 | 1.00 | 1.00 | 1.00 | 1.00 | 1.00 | 1.00 |
| | LPIPS↓ | 0.63 | 0.52 | 0.70 | 0.53 | 0.48 | 0.53 | 0.54 | 0.59 | 0.57 | 0.60 | 0.26 | 0.27 | 0.24 | 0.35 | 0.49 |
| Lotus-shin | PSNR↑ | 20.75 | 23.40 | 19.97 | 21.08 | 24.49 | 21.55 | 21.35 | 20.98 | 24.36 | 21.40 | 26.46 | 24.49 | 27.00 | 23.70 | 22.93 |
| | SSIM↑ | 1.00 | 1.00 | 1.00 | 1.00 | 1.00 | 1.00 | 1.00 | 1.00 | 1.00 | 1.00 | 1.00 | 1.00 | 1.00 | 1.00 | 1.00 |
| | LPIPS↓ | 0.54 | 0.65 | 0.70 | 0.51 | 0.53 | 0.51 | 0.50 | 0.58 | 0.67 | 0.58 | 0.30 | 0.26 | 0.28 | 0.31 | 0.50 |
| Metric3d-fs | PSNR↑ | 27.28 | 26.20 | 27.98 | 28.73 | 27.42 | 28.58 | 28.02 | 27.47 | 25.90 | 28.49 | 26.60 | 25.82 | 25.98 | 26.59 | 27.22 |
| | SSIM↑ | 1.00 | 1.00 | 1.00 | 1.00 | 1.00 | 1.00 | 1.00 | 1.00 | 1.00 | 1.00 | 1.00 | 1.00 | 1.00 | 1.00 | 1.00 |
| | LPIPS↓ | 0.39 | 0.54 | 0.40 | 0.33 | 0.41 | 0.33 | 0.32 | 0.40 | 0.58 | 0.39 | 0.28 | 0.27 | 0.28 | 0.25 | 0.37 |
| Metric3d-naive | PSNR↑ | 21.64 | 25.04 | 19.92 | 22.17 | 26.87 | 21.12 | 20.62 | 20.94 | 26.35 | 20.98 | 28.24 | 28.02 | 29.18 | 27.84 | 24.14 |
| | SSIM↑ | 1.00 | 1.00 | 1.00 | 1.00 | 1.00 | 1.00 | 1.00 | 1.00 | 1.00 | 1.00 | 1.00 | 1.00 | 1.00 | 1.00 | 1.00 |
| | LPIPS↓ | 0.65 | 0.52 | 0.71 | 0.53 | 0.47 | 0.51 | 0.52 | 0.60 | 0.55 | 0.60 | 0.26 | 0.26 | 0.24 | 0.24 | 0.47 |
| Metric3d-shin | PSNR↑ | 21.50 | 24.09 | 20.03 | 21.39 | 24.76 | 21.13 | 21.22 | 20.57 | 24.14 | 21.52 | 25.09 | 27.18 | 27.04 | 26.09 | 23.27 |
| | SSIM↑ | 1.00 | 1.00 | 1.00 | 1.00 | 1.00 | 1.00 | 1.00 | 1.00 | 1.00 | 1.00 | 1.00 | 1.00 | 1.00 | 1.00 | 1.00 |
| | LPIPS↓ | 0.63 | 0.63 | 0.68 | 0.51 | 0.53 | 0.50 | 0.51 | 0.58 | 0.68 | 0.58 | 0.32 | 0.26 | 0.29 | 0.27 | 0.50 |

| | | PSNR↑ | 27.35 | 25.85 | 27.41 | 28.09 | 27.41 | 28.73 | 28.20 | 27.08 | 26.85 | 28.44 | 26.74 | 22.98 | 25.75 | 25.90 | 26.91 |
|----------------|--------|-------|-------|-------|-------|-------|-------|-------|-------|-------|-------|-------|-------|-------|-------|-------------|-------------|
| ZoeDepth-fs | PSNR↑ | 1.00 | 21.45 | 25.84 | 20.61 | 21.24 | 26.54 | 21.04 | 20.86 | 21.04 | 26.50 | 21.03 | 28.71 | 25.02 | 28.44 | 27.51 | 23.99 |
| ZoeDepth-fs | SSIM↑ | 0.40 | 1.00 | 1.00 | 1.00 | 1.00 | 1.00 | 1.00 | 1.00 | 1.00 | 1.00 | 1.00 | 1.00 | 1.00 | 1.00 | 1.00 | 1.00 |
| ZoeDepth-naive | PSNR↑ | 0.40 | 0.55 | 0.47 | 0.32 | 0.41 | 0.31 | 0.33 | 0.39 | 0.54 | 0.39 | 0.27 | 0.34 | 0.28 | 0.26 | 0.38 | |
| ZoeDepth-naive | SSIM↑ | 0.65 | 1.00 | 0.53 | 0.71 | 0.54 | 0.45 | 0.52 | 0.53 | 0.59 | 0.55 | 0.60 | 0.26 | 0.34 | 0.25 | 0.26 | 0.48 |
| ZoeDepth-shin | PSNR↑ | 0.63 | 0.64 | 0.69 | 0.49 | 0.52 | 0.49 | 0.50 | 0.58 | 0.67 | 0.57 | 0.32 | 0.34 | 0.29 | 0.31 | 0.50 | |
| ZoeDepth-shin | SSIM↑ | 1.00 | 1.00 | 1.00 | 1.00 | 1.00 | 1.00 | 1.00 | 1.00 | 1.00 | 1.00 | 1.00 | 1.00 | 1.00 | 1.00 | 1.00 | |
| ZoeDepth-shin | LPIPS↓ | 0.63 | 0.64 | 0.69 | 0.49 | 0.52 | 0.49 | 0.50 | 0.58 | 0.67 | 0.57 | 0.32 | 0.34 | 0.29 | 0.31 | 0.50 | |

IV. CONCLUSION

To address the challenges of odometry and mapping in adverse environments, we develop a GS-based SLAM framework for monocular thermal image sequences. The system combines a robust learning-based tracking frontend with an efficient Gaussian Splatting mapping backend. The odometry module integrates a pretrained recurrent optical flow model with a pretrained monocular depth network, producing accurate camera poses and dense per-pixel depth for selected keyframes. Leveraging these reliable depth priors and pose estimates, the mapping backend constructs a global scene representation using Gaussian Splatting.

Compared with recent geometric and learning-based SLAM approaches, our method achieves superior tracking accuracy and robustness on two benchmark thermal SLAM datasets. Furthermore, GS-based mapping yields higher rendering performance than existing neural scene representation approaches.

We hope these results encourage further use of thermal imaging in SLAM and related applications. Currently, our GS mapping pipeline is limited to medium-scale environments (up to \sim 100 meters). In future work, we plan to scale the system to large-scale settings (on the order of kilometres), potentially through submap-based strategies [50].

REFERENCES

- [1] S. Daftry *et al.*, “Robust Vision-Based Autonomous Navigation, Mapping and Landing for MAVs at Night,” in *Proceedings of the 2018 International Symposium on Experimental Robotics*, J. Xiao, T. Kröger, and O. Khatib, Eds., Cham: Springer International Publishing, 2020, pp. 232–242. doi: 10.1007/978-3-030-33950-0_21.
- [2] S. Khattak, C. Papachristos, and K. Alexis, “Keyframe-based thermal–inertial odometry,” *J. Field Robot.*, vol. 37, no. 4, pp. 552–579, Jun. 2020, doi: 10.1002/rob.21932.
- [3] B. R. van Manen, V. Sluiter, and A. Y. Mersha, “FirebotSLAM: Thermal SLAM to Increase Situational Awareness in Smoke-Filled Environments,” *Sensors*, vol. 23, no. 17, Art. no. 17, Jan. 2023, doi: 10.3390/s23177611.
- [4] T. X. B. Nguyen, K. Rosser, and J. Chahl, “A review of modern thermal imaging sensor technology and applications for autonomous aerial navigation,” *J. Imaging*, vol. 7, no. 10, Art. no. 10, Oct. 2021, doi: 10.3390/jimaging7100217.
- [5] C. Campos, R. Elvira, J. J. G. Rodríguez, J. M. M. Montiel, and J. D. Tardós, “ORB-SLAM3: An accurate open-source library for visual, visual-inertial and multi-map SLAM,” *IEEE Trans. Robot.*, vol. 37, no. 6, pp. 1874–1890, Dec. 2021, doi: 10.1109/TRO.2021.3075644.
- [6] H. Bay, T. Tuytelaars, and L. Van Gool, “SURF: Speeded up robust features,” in *Computer Vision – ECCV 2006*, A. Leonardis, H. Bischof, and A. Pinz, Eds., in Lecture Notes in Computer Science. Berlin, Heidelberg: Springer, 2006, pp. 404–417. doi: 10.1007/11744023_32.
- [7] T. Mouats, N. Aouf, L. Chermak, and M. A. Richardson, “Thermal Stereo Odometry for UAVs,” *IEEE Sens. J.*, vol. 15, no. 11, pp. 6335–6347, Nov. 2015, doi: 10.1109/JSEN.2015.2456337.
- [8] P. V. K. Borges and S. Vidas, “Practical infrared visual odometry,” *IEEE Trans. Intell. Transp. Syst.*, vol. 17, no. 8, pp. 2205–2213, 2016.
- [9] B. Kitt, A. Geiger, and H. Lategahn, “Visual odometry based on stereo image sequences with RANSAC-based outlier rejection scheme,” in *2010 IEEE Intelligent Vehicles Symposium*, Jun. 2010, pp. 486–492. doi: 10.1109/IVS.2010.5548123.
- [10] Y. Wu *et al.*, “Improving autonomous detection in dynamic environments with robust monocular thermal SLAM system,” *ISPRS J. Photogramm. Remote Sens.*, vol. 203, pp. 265–284, Sep. 2023, doi: 10.1016/j.isprsjprs.2023.08.002.
- [11] R. Mur-Artal, J. M. M. Montiel, and J. D. Tardos, “ORB-SLAM: A versatile and accurate monocular SLAM system,” *IEEE Trans. Robot.*, vol. 31, no. 5, pp. 1147–1163, Oct. 2015, doi: 10.1109/TRO.2015.2463671.
- [12] Y. Wu *et al.*, “Catadioptric omnidirectional thermal odometry in dynamic environment,” *ISPRS J. Photogramm. Remote Sens.*, vol. 216, pp. 45–65, 2024.
- [13] C. Forster, Z. Zhang, M. Gassner, M. Werlberger, and D. Scaramuzza, “SVO: Semidirect visual odometry for monocular and multicamera systems,” *IEEE Trans. Robot.*, vol. 33, no. 2, pp. 249–265, Apr. 2017, doi: 10.1109/TRO.2016.2623335.
- [14] Y. Wang, H. Chen, Y. Liu, and S. Zhang, “Edge-Based Monocular Thermal-Inertial Odometry in Visually Degraded Environments,” *IEEE Robot. Autom. Lett.*, vol. 8, no. 4, pp. 2078–2085, Apr. 2023, doi: 10.1109/LRA.2023.3246381.
- [15] J. Chen, P. Hou, H. Zhao, Z. Cao, and J. Zhao, “EAMT-SLAM: Edge-Aided Monocular Thermal Sensor SLAM in Low-Illumination Environments,” *IEEE Sens. J.*, vol. 24, no. 20, pp. 33371–33386, Oct. 2024, doi: 10.1109/JSEN.2024.3452557.
- [16] X. Chen, W. Dai, J. Jiang, B. He, and Y. Zhang, “Thermal-depth odometry in challenging illumination conditions,” *IEEE Robot. Autom. Lett.*, vol. 8, no. 7, pp. 3988–3995, Jul. 2023, doi: 10.1109/LRA.2023.3271510.
- [17] W. Wang, Y. Hu, and S. Scherer, “TartanVO: A Generalizable Learning-based VO,” in *Proceedings of the 2020 Conference on Robot Learning*, Virtual: PMLR, Nov. 2020, pp. 1761–1772. Accessed: Nov. 25, 2024. [Online]. Available: <https://proceedings.mlr.press/v155/wang21h.html>
- [18] Z. Teed and J. Deng, “DROID-SLAM: Deep visual SLAM for monocular, stereo, and RGB-D cameras,” in *Ad-*

Advances in Neural Information Processing Systems, Curran Associates, Inc., 2021, pp. 16558–16569.

[19] U. Shin, K. Lee, B.-U. Lee, and I. S. Kweon, “Maximizing self-supervision from thermal image for effective self-supervised learning of depth and ego-motion,” *IEEE Robot. Autom. Lett.*, vol. 7, no. 3, pp. 7771–7778, Jun. 2022, doi: 10.1109/LRA.2022.3185382.

[20] M. R. U. Saputra, C. X. Lu, P. P. B. de Gusmao, B. Wang, A. Markham, and N. Trigoni, “Graph-Based Thermal-Inertial SLAM With Probabilistic Neural Networks,” *IEEE Trans. Robot.*, vol. 38, no. 3, pp. 1875–1893, Jun. 2022, doi: 10.1109/TRO.2021.3120036.

[21] S. Vidas, P. Moghadam, and M. Bosse, “3D Thermal Mapping of Building Interiors using an RGB-D and Thermal Camera,” presented at the IEEE International Conference on Robotics and Automation (ICRA), May 2013, pp. 2303–2310. doi: 10.1109/ICRA.2013.6630890.

[22] Y.-S. Shin and A. Kim, “Sparse Depth Enhanced Direct Thermal-Infrared SLAM Beyond the Visible Spectrum,” *IEEE Robot. Autom. Lett.*, vol. 4, no. 3, pp. 2918–2925, Jul. 2019, doi: 10.1109/LRA.2019.2923381.

[23] Y. Liu *et al.*, “ThermalGS: Dynamic 3D Thermal Reconstruction with Gaussian Splatting,” *Remote Sens.*, vol. 17, no. 2, p. 335, Jan. 2025, doi: 10.3390/rs17020335.

[24] J. Zhang *et al.*, “4DRT-SLAM: Robust SLAM in Smoke Environments using 4D Radar and Thermal Camera based on Dense Deep Learnt Features,” in *2023 IEEE International Conference on Cybernetics and Intelligent Systems (CIS) and IEEE Conference on Robotics, Automation and Mechatronics (RAM)*, Jun. 2023, pp. 19–24. doi: 10.1109/CIS-RAM55796.2023.10370026.

[25] W. Ye *et al.*, “PVO: Panoptic visual odometry,” in *2023 IEEE/CVF Conference on Computer Vision and Pattern Recognition (CVPR)*, Jun. 2023, pp. 9579–9589. doi: 10.1109/CVPR52729.2023.00924.

[26] Z. Teed, L. Lipson, and J. Deng, “Deep patch visual odometry,” in *Advances in Neural Information Processing Systems*, New Orleans, LA, USA: Curran Associates, Inc., Dec. 2023, pp. 39033–39051. Accessed: Nov. 21, 2024. [Online]. Available: https://proceedings.neurips.cc/paper_files/paper/2023/hash/7a c484b0f1a1719ad5be9aa8c8455fbb-Abstract-Conference.html

[27] B. Mildenhall, P. P. Srinivasan, M. Tancik, J. T. Barron, R. Ramamoorthi, and R. Ng, “NeRF: representing scenes as neural radiance fields for view synthesis,” *Commun. ACM*, vol. 65, no. 1, pp. 99–106, Jan. 2022, doi: 10.1145/3503250.

[28] X. Yang, H. Li, H. Zhai, Y. Ming, Y. Liu, and G. Zhang, “Vox-Fusion: Dense tracking and mapping with voxel-based neural implicit representation,” in *2022 IEEE International Symposium on Mixed and Augmented Reality (ISMAR)*, Oct. 2022, pp. 499–507. doi: 10.1109/ISMAR55827.2022.00066.

[29] A. Rosinol, J. J. Leonard, and L. Carlone, “NeRF-SLAM: Real-Time Dense Monocular SLAM with Neural Radiance Fields,” Oct. 24, 2022, *arXiv*: arXiv:2210.13641. doi: 10.48550/arXiv.2210.13641.

[30] G. Zhang, E. Sandström, Y. Zhang, M. Patel, L. V. Gool, and M. R. Oswald, “GIORIE-SLAM: Globally optimized RGB-only implicit encoding point cloud SLAM,” May 27, 2024, *arXiv*: arXiv:2403.19549. doi: 10.48550/arXiv.2403.19549.

[31] J. Naumann, B. Xu, S. Leutenegger, and X. Zuo, “NeRF-VO: Real-time sparse visual odometry with neural radiance fields,” *IEEE Robot. Autom. Lett.*, vol. 9, no. 8, pp. 7278–7285, Aug. 2024, doi: 10.1109/LRA.2024.3421192.

[32] B. Kerbl, G. Kopanas, T. Leimkühler, and G. Drettakis, “3D Gaussian splatting for real-time radiance field rendering,” *ACM Trans. Graph.*, vol. 42, no. 4, pp. 139–1, 2023.

[33] B. Huang, Z. Yu, A. Chen, A. Geiger, and S. Gao, “2D Gaussian splatting for geometrically accurate radiance fields,” in *ACM SIGGRAPH 2024 Conference Papers*, in SIGGRAPH ’24. New York, NY, USA: Association for Computing Machinery, Jul. 2024, pp. 1–11. doi: 10.1145/3641519.3657428.

[34] Z. Ye, W. Li, S. Liu, P. Qiao, and Y. Dou, “AbsGS: Recovering fine details in 3D Gaussian splatting,” in *Proceedings of the 32nd ACM International Conference on Multimedia*, in MM ’24. New York, NY, USA: Association for Computing Machinery, Oct. 2024, pp. 1053–1061. doi: 10.1145/3664647.3681361.

[35] H. Matsuki, R. Murai, P. H. J. Kelly, and A. J. Davison, “Gaussian splatting SLAM,” in *2024 IEEE/CVF Conference on Computer Vision and Pattern Recognition (CVPR)*, Jun. 2024, pp. 18039–18048. doi: 10.1109/CVPR52733.2024.01708.

[36] N. Keetha *et al.*, “SplaTAM: Splat, track & map 3D Gaussians for dense RGB-D SLAM,” in *2024 IEEE/CVF Conference on Computer Vision and Pattern Recognition (CVPR)*, Jun. 2024, pp. 21357–21366. doi: 10.1109/CVPR52733.2024.02018.

[37] H. Huang, L. Li, H. Cheng, and S.-K. Yeung, “Photo-SLAM: Real-time Simultaneous Localization and Photorealistic Mapping for Monocular Stereo and RGB-D Cameras,” in *Proceedings of the IEEE/CVF Conference on Computer Vision and Pattern Recognition*, 2024, pp. 21584–21593.

[38] P. Jiang, H. Liu, X. Li, T. Wang, F. Zhang, and J. M. Buhmann, “TAMBRIDGE: Bridging Frame-Centered Tracking and 3D Gaussian Splatting for Enhanced SLAM,” May 30, 2024, *arXiv*: arXiv:2405.19614. doi: 10.48550/arXiv.2405.19614.

[39] E. Sandström *et al.*, “Splat-SLAM: globally optimized RGB-only SLAM with 3D Gaussians,” May 26, 2024, *arXiv*: arXiv:2405.16544. doi: 10.48550/arXiv.2405.16544.

[40] C. Doer and G. F. Trommer, “Radar visual inertial odometry and radar thermal inertial odometry: Robust navigation even in challenging visual conditions,” in *2021 IEEE/RSJ International Conference on Intelligent Robots and Systems (IROS)*, Prague, Czech Republic: IEEE, Sep. 2021, pp. 331–338. doi: 10.1109/IROS51168.2021.9636799.

[41] A. J. Lee, Y. Cho, Y. Shin, A. Kim, and H. Myung, “ViViD++: Vision for Visibility Dataset,” *IEEE Robot. Autom. Lett.*, vol. 7, no. 3, pp. 6282–6289, Jul. 2022, doi: 10.1109/LRA.2022.3168335.

[42] H. Gil, M.-H. Jeon, and A. Kim, “Fieldscale: Locality-Aware Field-Based Adaptive Rescaling for Thermal Infrared Image,” *IEEE Robot. Autom. Lett.*, vol. 9, no. 7, pp. 6424–6431, Jul. 2024, doi: 10.1109/LRA.2024.3406054.

[43] Z. Teed and J. Deng, “RAFT: Recurrent All-Pairs Field Transforms for Optical Flow,” in *Computer Vision – ECCV 2020*, A. Vedaldi, H. Bischof, T. Brox, and J.-M. Frahm, Eds., in *Lecture Notes in Computer Science*, vol. 12347. Cham: Springer International Publishing, 2020, pp. 402–419. Ac-

cessed: Aug. 20, 2024. [Online]. Available: https://link.springer.com/10.1007/978-3-030-58536-5_24

[44] W. Yin *et al.*, “Metric3D: Towards Zero-shot Metric 3D Prediction from A Single Image,” in *2023 IEEE/CVF International Conference on Computer Vision (ICCV)*, Oct. 2023, pp. 9009–9019. doi: 10.1109/ICCV51070.2023.00830.

[45] L. Yang, B. Kang, Z. Huang, X. Xu, J. Feng, and H. Zhao, “Depth Anything: Unleashing the Power of Large-Scale Unlabeled Data,” in *2024 IEEE/CVF Conference on Computer Vision and Pattern Recognition (CVPR)*, Jun. 2024, pp. 10371–10381. doi: 10.1109/CVPR52733.2024.00987.

[46] S. F. Bhat, R. Birk, D. Wofk, P. Wonka, and M. Müller, “ZoeDepth: Zero-shot Transfer by Combining Relative and Metric Depth,” Feb. 23, 2023, *arXiv*: arXiv:2302.12288. doi: 10.48550/arXiv.2302.12288.

[47] R. Ranftl, A. Bochkovskiy, and V. Koltun, “Vision Transformers for Dense Prediction,” in *2021 IEEE/CVF International Conference on Computer Vision (ICCV)*, Oct. 2021, pp. 12159–12168. doi: 10.1109/ICCV48922.2021.01196.

[48] Z. Zhang and D. Scaramuzza, “A tutorial on quantitative trajectory evaluation for visual(-inertial) odometry,” in *IEEE/RSJ Intl. Conf. on Intelligent Robots and Systems (IROS)*, Madrid, Spain, Oct. 2018, pp. 7244–7251. doi: 10.1109/IROS.2018.8593941.

[49] X. Gao, R. Wang, N. Demmel, and D. Cremers, “LDSO: Direct Sparse Odometry with Loop Closure,” in *2018 IEEE/RSJ International Conference on Intelligent Robots and Systems (IROS)*, Oct. 2018, pp. 2198–2204. doi: 10.1109/IROS.2018.8593376.

[50] W. Hess, D. Kohler, H. Rapp, and D. Andor, “Real-time loop closure in 2D LIDAR SLAM,” in *2016 IEEE International Conference on Robotics and Automation (ICRA)*, Stockholm, Sweden, May 2016, pp. 1271–1278. doi: 10.1109/ICRA.2016.7487258.